Published in final edited form as:
Magn Reson Med. 2010 October ; 64(4): 1171–1181. doi:10.1002/mrm.22434.

Max CAPR: High-Resolution 3D Contrast-Enhanced MR Angiography With Acquisition Times Under 5 Seconds

Clifton R. Haider, **Eric A. Borisch**, **James F. Glockner**, **Petrice M. Mostardi**, **Phillip J. Rossman**, **Phillip M. Young**, and **Stephen J. Riederer***
MR Research Laboratory, Mayo Clinic, Rochester, Minnesota, USA

Abstract

High temporal and spatial resolution is desired in imaging of vascular abnormalities having short arterial-to-venous transit times. Methods that exploit temporal correlation to reduce the observed frame time demonstrate temporal blurring, obfuscating bolus dynamics. Previously, a Cartesian acquisition with projection reconstruction-like (CAPR) sampling method has been demonstrated for three-dimensional contrast-enhanced angiographic imaging of the lower legs using two-dimensional sensitivity-encoding acceleration and partial Fourier acceleration, providing 1mm isotropic resolution of the calves, with 4.9-sec frame time and 17.6-sec temporal footprint. In this work, the CAPR acquisition is further undersampled to provide a net acceleration approaching 40 by eliminating all view sharing. The tradeoff of frame time and temporal footprint in view sharing is presented and characterized in phantom experiments. It is shown that the resultant 4.9-sec acquisition time, three-dimensional images sets have sufficient spatial and temporal resolution to clearly portray arterial and venous phases of contrast passage. It is further hypothesized that these short temporal footprint sequences provide diagnostic quality images. This is tested and shown in a series of nine contrast-enhanced MR angiography patient studies performed with the new method.

Keywords

contrast-enhanced MR angiography; 2D-SENSE; 2D-partial Fourier; temporal footprint; view sharing; single phase

Contrast-enhanced MR angiography (CE-MRA) has become a widely accepted method for imaging of the cardiovascular system (1,2). Although work a decade ago was directed toward generating a single arterial-phase image of a given region with high spatial resolution; e.g., (3,4), there has also been continuing interest in performing time-resolved imaging. One approach for doing this is to simply repeat the MRA pulse sequence and reconstruct an individual two-dimensional (2D) or three-dimensional (3D) image for each replication (5–8). Another approach is to employ view sharing (9), in which data are shared from one image to the next in the time series. This can be further refined so that central *k*-space is sampled more frequently than the *k*-space periphery (10–14). As described previously (9), although view sharing provides a numerical increase in the image frame rate, defined as the rate at which reconstructions are performed, this does not directly correspond to increased temporal resolution because of the commonality of at least some of the

*Correspondence to: Stephen J. Riederer, Ph.D., MR Research Laboratory, Mayo Clinic, 200 First Street, SW, Rochester, MN 55905., riederer@mayo.edu.

Additional Supporting Information may be found in the online version of this article.

underlying data from one image to the next, leading to temporal correlation. This has also been described for the highly constrained back projection (HYPR) technique (15–17).

Another area of investigation over the last decade has been the ongoing development of projection reconstruction methods in MRI (18,19). An intrinsic advantage of projection reconstruction methods is the robustness to undersampling, defined as the use of fewer projections than might be stipulated by the Nyquist criterion.

Simultaneous with these advances in time-resolved techniques has been the development of parallel imaging (20–22). This has been applied to CE-MRA, with one-dimensional acceleration factors (R) typically ranging from $R = 2–3$ (20,23–27) and 2D acceleration (28) as high as $R = 4–8$ (29–33). In one specific implementation, a Cartesian acquisition with projection-reconstruction-like sampling, or "CAPR," has been developed in which a projection reconstruction–like sampling pattern is used in the 2D phase-encoding plane of a 3D Fourier transform (3DFT) acquisition to provide consistency of the *k*-space sampling pattern from one image to the next and a benign point-spread function (34,35).

The purpose of this work is to describe a modification of the above CAPR technique in which only a subset of the normally acquired samples is used for image reconstruction. This process is the Cartesian analog to the undersampling of projections in standard projection reconstruction imaging. The additional 2.5-fold undersampling, coupled with accelerations already incorporated into CAPR of 2D sensitivity encoding (SENSE) and 2D homodyne (HD), provides a net acceleration purely due to *k*-space undersampling approaching 40. As implemented here for CE-MRA, this yields an acquisition time less than 5 sec per unsubtracted, high-spatial-resolution, 3D image. We believe these acquisition times are the smallest ever demonstrated for contrast-enhanced MR angiograms of the peripheral vasculature of this quality. This work is an expansion of a previously reported abstract (36), and we now present experimental studies in phantoms and results from a series of patients with peripheral vascular disease.

MATERIALS AND METHODS

Description of the Basic Sequence

As a reference the basic CAPR sequence is shown in Fig. 1. In Fig. 1a, the k_Y-k_Z phase encoding plane is separated into two sections: (i) a fully sampled central disk and (ii) an outer annulus divided into 2-fold azimuthally undersampled "vanes." Typically, 32 vanes are used, separated by evenly spaced gaps. The outer corners of the k_Y-k_Z plane are not sampled so as to make spatial resolution approximately isotropic (37). All sampling is done on a Cartesian grid, but only those grid points falling within the central disk and the vanes are sampled in the acquisition. Data on the grid points within the unsampled gaps between the vanes are estimated using 2D HD processing (38). The vanes are decomposed into sets, four shown here in color. The temporal play-out is shown in (Fig. 1c), with sampling of central *k*-space alternated with cyclic sampling of one vane set. For all colored regions, an elliptical centric phase-encoding order (3) is used. Sorting of data for reconstruction of two consecutive CAPR frames is shown in Fig. 1d,e, with view sharing done over the vane sets.

The essence of Max CAPR is to further undersample the k_Y-k_Z plane by using only one vane set in the image reconstruction. This more sparsely sampled k_Y-k_Z space for Max CAPR is illustrated in Fig. 1b. The same temporal play-out of phase encodings is used as for CAPR (Fig. 1c), but the data selected for image reconstruction are restricted to only one of the four vane sets, as illustrated in Fig. 1f,g. The Max CAPR and CAPR images reconstructed for timeframe #1 have the same central orange region and red vane set sampling, but Max CAPR is undersampled azimuthally because only one vane set is used,

while for CAPR the previous three vane sets (black, green, blue) are used in reconstruction. For timeframe #2 for Max CAPR, central *k*-space is resampled and the next vane set (here black) is used. With CAPR the same holds, but additionally the green, blue, and red vane sets are shared from frame #1 to frame #2. For both CAPR and Max CAPR, the unsampled points of k_Y-k_Z space in the annular region diagonally opposite the points in the sampled vanes are estimated using 2D HD processing. For Max CAPR, any other unsampled points are simply zero-filled.

To compute acceleration, take as a reference the circumscribing circle of the k_Y-k_Z sampling pattern of Fig. 1a. Acceleration due to 2D HD is generally 1.7 to 1.9, with 1.8 a typical value. This acceleration is dependent on the size of the central region. As the radius of the central region increases, the accuracy of the phase map estimate used for HD reconstruction improves. However, this is offset by a reduction in the HD-related acceleration. We have found empirically that a central radius in the range of 0.30–0.35 of the full *k*-space sampling radius works well in imaging the calves and provides a good compromise between these competing effects (39). Independently of HD, 2D SENSE can be applied, with a typical acceleration being $R = R_Y \times R_Z = 4 \times 2 = 8$. Combined, 2D SENSE and 2D HD provide a typical net acceleration of 14.6. Finally, use of only one versus the full four vane sets typically provides additional undersampling of 2.5–2.8, depending on the radius of the central orange disk. This provides a net acceleration of approximately 40.

Pulse Sequence Parameters

Acquisitions were targeted to provide 1mm isotropic spatial resolution over a field of view (FOV) allowing bilateral imaging of the calves, with temporal resolution of 5 sec to distinguish the arterial from the venous phase of contrast passage. Typical parameters for CE-MRA of the calves are coronal orientation, phase encoding done along the left-right FOV of 32 cm, and slice encoding done along the anterior-posterior (A/P) FOV of 13.2 cm. Combining these FOV values with 1mm sampling subject to approximately $\pi/4$ reduction by not sampling the corners of k_Y-k_Z space leads to a requirement of approximately 33,000 samples, or a 193-sec acquisition time, assuming a gradient echo pulse sequence with a pulse repetition time of 5.85 msec as used here. Other sequence parameters are summarized in Table 1. The temporal footprint is defined as the time over which data are acquired to form an image which for Max CAPR is equal to the frame time. As seen in the last two columns, this is 4.9 sec for the in vivo results reported here.

Phantom Experiments

Experiments using phantoms were devised to assess possible artifacts caused within the phase-encoding plane due to the additional azimuthal undersampling provided by Max CAPR versus CAPR. Three long tubes of 3, 5, and 10mm diameter were filled with a 100:1 dilution of water to gadolinium (Gd) contrast agent to mimic contrast- enhanced blood vessels. The tubes were placed along the frequency-encoding (k_X) direction within the FOV described above and were imaged using 3DFT acquisition with (i) a fully sampled k_Y-k_Z space but with the corners eliminated, and (ii) the CAPR and the new Max CAPR samplings with SENSE accelerations (R) of $R = 1, 2, 4$, and 8. Details are provided in Table 1. For (ii) 2D HD was also performed for CAPR and Max CAPR. Also, for (ii) the number of points within the central orange region of Fig. 1 was kept fixed at 400 for all SENSE accelerations. Because the *k*-space sampling distance increases with increased SENSE acceleration, this caused the radius of the central region, expressed as a fraction of the full radius of the vanes, to take on increasing values of 0.11, 0.15, 0.22, and 0.31 for SENSE accelerations of 1, 2, 4, and 8, respectively.

Additional experiments were devised to assess the ability of the Max CAPR technique to portray the leading and trailing edges of a simulated, advancing contrast bolus using the setup of Mostardi et al. (40). A 400mm-long vial 22mm in diameter, filled with diluted Gd contrast material, was moved along the amplitude of static field in a tabletop track, using a computer-controlled stepper motor, allowing the position and velocity of the vial to be precisely known throughout the scan duration. This orientation mimics the passage of contrast material along the major vessels of the calves in a coronal MRA acquisition. The CAPR acquisition was performed continuously during the transit of the vial at a velocity of 16.0 mm/sec across the imaging FOV, and CAPR and Max CAPR reconstructions were generated. The images were assessed for the level of artifact at the leading and trailing edges of the phantom along the direction of motion.

In Vivo Studies

Time-resolved 3D CE-MRA studies using Max CAPR were performed on 10 human volunteers to assess performance in imaging the vasculature of the lower legs. Additionally, a controlled study with fixed parameters was performed on nine consecutive patients referred from our CT angiography practice who were suspected of having peripheral vascular disease of one or both lower legs. Imaging was done using a 3.0-T MRI system (Signa 14.0; GE Healthcare, Milwaukee, WI). All studies were Health Insurance Portability and Accountability Act (HIPAA) compliant and approved by our institutional review board, with informed written consent obtained from all subjects. Scan parameters were similar to those of the phantom studies and are shown in Table 1. 2D SENSE acceleration with $R = 8 = 4$ (left-right) × 2 (A/P) was performed using an eight-element coil array, which circumscribes the calves (35). For all studies, 20 mL of gadobenate dimeglumine contrast agent (MultiHance; Bracco Diagnostics, Princeton, NJ) was injected into the right antecubital vein at 3 mL/sec, followed by 20 mL of saline at 3 mL/sec with an electronic injector. Images were reconstructed using both the CAPR and Max CAPR sorting of Fig. 1. For CAPR, the first frame formed from the *k*-space center and all four vanes sets was used as a mask and subtracted from all subsequent frames for removal of background. For Max CAPR, the center and first vane set of one color of Fig. 1a were subtracted from subsequent frames formed from the center and vane set of that same color; i.e., there were in effect four separate masks. Contrast was injected only after the above contrast-free images were first acquired. The entire acquisition typically extended for about 90 sec, including capture of the precontrast subtraction mask, arterial phase, and venous phase. All reconstructions were performed automatically offline using distributed computing. The reconstructed DICOM images were available for review on the host scanner console within 2 min after scan completion, allowing nearly immediate clinical review (41).

Radiologic Evaluation

Results from the CAPR and Max CAPR acquisitions from the series of nine patient studies were used to test the hypothesis that Max CAPR provides diagnostic quality images of vasculature of the calves. Results from the CAPR and Max CAPR acquisitions for each of the nine patients were independently assessed by two collaborating body radiologists (J.F.G., P.M.Y.), based upon six radiologic evaluation categories relevant for accelerated time-resolved MRA. Each category was defined on a 4-point scale, with a score of 1 generally considered non-diagnostic and a score of 4 considered excellent. These are further defined in Table 2. Assessments were done blindly. That is, there was no identification whether a study was reconstructed using CAPR or Max CAPR, and a paired CAPR and Max CAPR study for a given subject was separated by at least five other studies in the evaluation. For each study, the full-volume maximum intensity projection (MIP) and the individual coronal partitions were available for each timeframe. Additionally, the viewer was able to

reorient the 3D data at arbitrary angulation and perform MIPs over a limited spatial extent of the volume.

The hypothesis was tested by determination of possible significance between the scores for Max CAPR against a hypothetical marginal clinical examination, defined as one receiving a score of 2 for all six evaluation categories. This was tested using the Wilcoxon signed rank test, with significance taken as $P < 0.05$ (42). For all six categories, Max CAPR was also compared with CAPR, and a possible difference in performance was also tested, using the same test and definition of significance.

RESULTS

Figure 2 shows the operating curves formed by relating the image update time to temporal footprint for a 4- and 8-fold accelerated view-shared CAPR sequence and an 8-fold accelerated Max CAPR sequence. The “Nm” indicates “m” vane sets are used in the sampling, with N4 being that presented in Fig. 1 and used throughout this work. The numerical reduction in image update time allowed by view sharing in the CAPR sequence causes a leftward shift along a given curve. Along with this, there is an increase in the temporal footprint. On the other hand, an increase in the SENSE acceleration causes an entire curve to be shifted down and to the left. The Max CAPR sequence forms the line of identity because the image update time is exactly equal to the temporal footprint.

Figure 3 shows cross-sectional images of the tube phantoms and demonstrates the effect for the Max CAPR results that as the net acceleration increases, the level of “starburst-like” undersampling artifact decreases. This is a consequence of the radius of the central orange region increasing with increased SENSE acceleration. Consequently, the level of vessel sharpness improves, most dramatically for the largest tube.

Figure 4 is a composite showing images taken from different timeframes of the leading and trailing edges of the moving bolus phantom for CAPR and Max CAPR reconstructions. CAPR Delay 0 (Fig. 4a) corresponds to the selection of phase encodes shown in Fig. 1d,e, in which the vane sets used for reconstruction are composed of one measured after and three measured prior to the central orange views (40). CAPR Delay 3 (Fig. 4b), not shown in Fig. 1, is the case in which all four vane sets used in reconstruction are measured after the central orange views (40). Max CAPR (Fig. 4c) corresponds to the reconstruction of Fig. 1f,g. In Fig. 4, the known edge positions at the time of measurement of the centralmost phase encode in all six cases are marked with the two vertical dashed lines. For each image in Fig. 4, the play-out of the colored regions of *k*-space (Fig. 1) for that image is matched to the bolus leading or trailing edge position by the colored blocks shown. For CAPR Delay 0 (Fig. 4a) and Delay 3 (Fig. 4b), this sequence of blocks extends beyond what is shown in the figure and is truncated for brevity. As seen, results with CAPR Delay 0 (Fig. 4a) provide good depiction of the bolus leading edge but have artifactual signal at the trailing edge (vertical arrows), called “persistence artifact.” Conversely, results with CAPR Delay 3 (Fig. 4b) have artifactual signal in advance of the bolus (vertical arrows), called “anticipation artifact,” but negligible artifact at the trailing edge. Max CAPR (Fig. 4c) simultaneously has the desirable properties of good portrayal of both the leading and trailing edges.

Figure 5 is a comparison of the portrayal of the leading edge of the advancing contrast bolus taken from a study of the lower legs of a volunteer, using 2D SENSE $R = 8$. Full coronal MIPs are shown for CAPR (Fig. 5a) and Max CAPR (Fig. 5b). Enlargements of the areas within black boxes are shown for the subject’s right leg for CAPR (Fig. 5c) and Max CAPR (Fig. 5d) and left leg for CAPR (Fig. 5e) and Max CAPR (Fig. 5f). Regions within the black boxes in (Fig. 5c) and (Fig. 5d) demonstrate the increased noise level for CAPR. As a

consequence of the reduced noise level, clearer portrayal of the bolus leading edge for Max CAPR is seen in (Fig. 5f, arrows) versus CAPR (Fig. 5e).

Figure 6 shows plots of the scores of the two reviewers, identified in different colors, for Max CAPR (M) and CAPR (C) for each of the six evaluation categories. The mean and standard deviations of the aggregate scores are shown in Table 3. For all six categories, the performance of Max CAPR, as well as CAPR, was significantly higher than 2, and the hypothesis is thus proven to be true. For categories I (image artifact) and IV (vessel sharpness), the performance of CAPR was superior statistically to Max CAPR, probably as a consequence of the increased degree of sampling of the annular region of *k*-space shown in Fig. 1. For the other categories (II, III, V, VI), there was no statistically significant difference between Max CAPR and CAPR.

Figures 7 and 8 show results from the patient studies. Figure 7 is a comparison from patient #5 of CAPR and Max CAPR. Figure 8, taken from patient #8, illustrates the intrinsic spatial and temporal resolution of Max CAPR. Supplementary videos V1 and V2 are taken from the study of Fig. 7 and V3 and V4 from that of Fig. 8. Movies are played back at approximately the acquired frame rate, with one full rotation equal to 5 sec.

DISCUSSION

This work demonstrates that a non-view-shared Cartesian 3D contrast-enhanced MR angiographic technique can provide diagnostic-quality 1mm isotropic imaging of both calves, with an acquisition time per image under 5 sec. This acquisition time is approximately 4 to 15× smaller than those reported in other works of CE-MRA using similar fields of view and comparable or even coarser spatial resolution (39,43,44). In the patient series studied, continuous acquisition at this frame time allowed clear differentiation of the arterial and venous phases. The level of artifact, primarily manifest as subtle, starburst-like patterns emanating from luminal signals in the transverse images, was considered to be no worse than minor in 15/16 evaluations. No other image artifacts other than this pattern were observed. This is attributed to the full radial and azimuthal coverage of the Max CAPR *k*-space sampling pattern, the resulting isotropic spatial point spread function, and the robust nature of the 2D acceleration methods used. The overall image quality of the Max CAPR patient studies was rated excellent in 9/18 and good in the remaining 9/18 evaluations. A more detailed clinical evaluation is beyond the scope of this work, but the results presented suggest the ability of Max CAPR to accurately portray the common findings of stenosis (Fig. 7) and complex vascular-filling patterns (Fig. 8).

Compared to CAPR sampling (Fig. 1a) because Max CAPR (Fig. 1b) fundamentally undersamples the k_Y-k_Z phase encoding plane, some degree of artifact due to undersampling is expected. This can be controlled by two aspects of the sampling pattern. First is the number of vane sets used, four in this work. Use of fewer vane sets, each spanning the full 2π radians of *k*-space, would result in an increased number of vanes for each Max CAPR image and somewhat less acceleration but also less artifact. A second aspect of the sampling pattern critical for controlling artifact is the size of the central region of *k*-space sampling. As shown in Fig. 3, as this central area increases, the level of radial streak artifact decreases. Both of these trends of reduced artifact with an increased number of vanes and reduced artifact with more extensive central sampling follow from the theory of projection reconstruction sampling (45). For this work, the combination of four vane sets and a central region with radius approximately 30% of the radius of full *k*-space sampling provided good performance.

Sharing of data from frame to frame introduces temporal correlation, as has been described for both Cartesian (9) and non-Cartesian (15,16,46) sequences. This can cause phenomena occurring in one frame to be artifactually manifest in other frames and, in the case of CE-MRA, lead to anticipation or persistence artifact emanating from the contrast-enhanced vasculature (40). The removal of view sharing in Max CAPR eliminates all susceptibility to such frame-to-frame-related artifacts and has performance benefits of single-phase EC acquisitions (3). Removal of view sharing also eliminates the ambiguity in numerical calculation of acceleration in time-resolved sequences by equating the image update time with total acquisition time per frame. Although the reduced acquisition time of Max CAPR versus CAPR did not provide a statistically significant improvement in performance for arterial-to-venous separation (category II) in this series, this may be important in specific patient groups who have rapid arterial-to-venous transit, such as those with ischemic disease of the extremities or arteriovenous malformations. Small absolute acquisition times, as allowed by Max CAPR undersampling, can also be important for multistation CE-MRA of the extended peripheral vasculature. In this case, the acquisition time per station must be necessarily kept small to allow the table motion to track the advancing contrast bolus (47,48).

Although not statistically significant, Max CAPR tended to provide superior portrayal of the leading edge of the contrast bolus versus CAPR (Fig. 5). Although SNR was not measured with any view-shared acquisition, including CAPR, any phase-encoding views measured of a region prior to contrast arriving in that region will contribute only noise to the reconstructed values in that region. Similarly, measurement of all peripheral *k*-space vane sets after the central views can cause artifactual anticipation artifact, as seen for the leading edge in Fig. 4b (40). This sharing of data results in decreased SNR that reduces vessel conspicuity and continuity at the vessel leading edge. In vessels that are enhanced throughout the entire image acquisition time, there will be no benefit of Max CAPR versus CAPR because the unsampled vane sets are simply zero filled for Max CAPR, causing the average signal to be diminished compared to the fully sampled CAPR case.

In this work, *k*-space undersampling factors nearly 40-fold were shown in phantom experiments and the calves to be robust to noise amplification and degradation of spatial resolution. This is possible for several reasons. First, the use of 2D versus one-dimensional methods causes less noise amplification for a given acceleration (14,26–28,30,32,34,49,50). Second, in the imaging of a transient phenomenon such as passage of a contrast agent, acceleration can provide a compensatory effect on SNR loss and an improvement in spatial resolution (51–53). Third, this specific application to CE-MRA of the peripheral vasculature benefitted from the use of multielement radiofrequency receiver arrays designed for circumferential placement around the legs and well suited to 2D SENSE (35). The acceleration provided by Max CAPR could also be used to increase the spatial resolution or decrease the acquisition time in standard single-phase imaging. This is not possible with methods that rely on spatiotemporal correlations (54) or iterative techniques that rely on temporal composites (15,46,55).

In summary, we have demonstrated a method for combining 2D acceleration methods and additional undersampling of the Cartesian phase-encoding plane to generate 3D contrast-enhanced MRA images of the peripheral vasculature, with an acquisition time per image of less than 5 sec. Results in patients portray the vasculature with high spatial resolution, and the temporal resolution of the technique allows clear separation of the arterial and venous phases, as well as the delineation of complex filling patterns.

Supplementary Material

Refer to Web version on PubMed Central for supplementary material.

Acknowledgments

The authors acknowledge Kathy J. Brown, Roger C. Grimm, Christine C. La Plante, Thanila A. Macedo, M.D., and Terri J. Vrtiska, M.D., for their assistance.

References

1. Prince MR, Yucel EK, Kaufman JA, Harrison DC, Geller SC. Dynamic gadolinium-enhanced three-dimensional abdominal MR arteriography. J Magn Reson Imaging. 1993; 3:877–881. [PubMed: 8280977]
2. Zhang H, Maki JH, Prince MR. 3D contrast-enhanced MR angiography. J Magn Reson Imaging. 2007; 25:13–25. [PubMed: 17154188]
3. Wilman AH, Riederer SJ, King BF, Debbins JP, Rossman PJ, Ehman RL. Fluoroscopically triggered contrast-enhanced three-dimensional MR angiography with elliptical centric view order: application to the renal arteries. Radiology. 1997; 205:137–146. [PubMed: 9314975]
4. Huston J 3rd, Fain SB, Riederer SJ, Wilman AH, Bernstein MA, Busse RF. Carotid arteries: maximizing arterial to venous contrast in fluoroscopically triggered contrast-enhanced MR angiography with elliptic centric view ordering. Radiology. 1999; 211:265–273. [PubMed: 10189482]
5. Wang Y, Johnston DL, Breen JF, Huston J 3rd, Jack CR, Julsrud PR, Kiely MJ, King BF, Riederer SL, Ehman RL. Dynamic MR digital subtraction angiography using contrast enhancement, fast data acquisition, and complex subtraction. Magn Reson Med. 1996; 36:551–556. [PubMed: 8892206]
6. Schoenberg SO, Bock M, Knopp MV, Essig M, Laub G, Hawighorst H, Zuna I, Kallinowski F, van Kaick G. Renal arteries: optimization of three-dimensional gadolinium-enhanced MR angiography with bolus-timing-independent fast multiphase acquisition in a single breath hold. Radiology. 1999; 211:667–679. [PubMed: 10352590]
7. Sodickson DK, McKenzie CA, Li W, Wolff S, Manning WJ, Edelman RR. Contrast-enhanced 3D MR angiography with simultaneous acquisition of spatial harmonics: a pilot study. Radiology. 2000; 217:284–289. [PubMed: 11012458]
8. Finn JP, Baskaran V, Carr JC, McCarthy RM, Pereles FS, Kroeker R, Laub GA. Thorax: low-dose contrast-enhanced three-dimensional MR angiography with subsecond temporal resolution—initial results. Radiology. 2002; 224:896–904. [PubMed: 12202730]
9. Riederer SJ, Tasciyan T, Farzaneh F, Lee JN, Wright RC, Herfkens RJ. MR fluoroscopy: technical feasibility. Magn Reson Med. 1988; 8:1–15. [PubMed: 3173063]
10. van Vaals JJ, Brummer ME, Dixon WT, Tuithof HH, Engels H, Nelson RC, Gerety BM, Chezmar JL, den Boer JA. “Keyhole” method for accelerating imaging of contrast agent uptake. J Magn Reson Imaging. 1993; 3:671–675. [PubMed: 8347963]
11. Parrish T, Hu X. Continuous update with random encoding (CURE): a new strategy for dynamic imaging. Magn Reson Med. 1995; 33:326–336. [PubMed: 7760701]
12. Doyle M, Walsh EG, Blackwell GG, Pohost GM. Block regional interpolation scheme for k-space (BRISK): a rapid cardiac imaging technique. Magn Reson Med. 1995; 33:163–170. [PubMed: 7707905]
13. Korosec FR, Frayne R, Grist TM, Mistretta CA. Time-resolved contrast-enhanced 3D MR angiography. Magn Reson Med. 1996; 36:345–351. [PubMed: 8875403]
14. Fink C, Ley S, Kroeker R, Requardt M, Kauczor HU, Bock M. Time-resolved contrast-enhanced three-dimensional magnetic resonance angiography of the chest: combination of parallel imaging with view sharing (TREAT). Invest Radiol. 2005; 40:40–48. [PubMed: 15597019]
15. Mistretta CA, Wieben O, Velikina J, Block W, Perry J, Wu Y, Johnson K. Highly constrained backprojection for time-resolved MRI. Magn Reson Med. 2006; 55:30–40. [PubMed: 16342275]

16. Huang Y, Wright GA. Time-resolved MR angiography with limited projections. Magn Reson Med. 2007; 58:316–325. [PubMed: 17654575]
17. Keith L, Kecskemeti S, Velikina J, Mistretta C. Simulation of relative temporal resolution of time-resolved MRA sequences. Magn Reson Med. 2008; 60:398–404. [PubMed: 18666099]
18. Peters DC, Korosec FR, Grist TM, Block WF, Holden JE, Vigen KK, Mistretta CA. Undersampled projection reconstruction applied to MR angiography. Magn Reson Med. 2000; 43:91–101. [PubMed: 10642735]
19. Du J, Korosec FR, Thornton FJ, Grist TM, Mistretta CA. High-resolution multistation peripheral MR angiography using undersampled projection reconstruction imaging. Magn Reson Med. 2004; 52:204–208. [PubMed: 15236388]
20. Sodickson DK, Manning WJ. Simultaneous acquisition of spatial harmonics (SMASH): fast imaging with radiofrequency coil arrays. Magn Reson Med. 1997; 38:591–603. [PubMed: 9324327]
21. Pruessmann KP, Weiger M, Scheidegger MB, Boesiger P. SENSE: sensitivity encoding for fast MRI. Magn Reson Med. 1999; 42:952–962. [PubMed: 10542355]
22. Griswold MA, Jakob PM, Heidemann RM, Nittka M, Jellus V, Wang J, Kiefer B, Haase A. Generalized autocalibrating partially parallel acquisitions (GRAPPA). Magn Reson Med. 2002; 47:1202–1210. [PubMed: 12111967]
23. Weiger M, Pruessmann KP, Kassner A, Roditi G, Lawton T, Reid A, Boesiger P. Contrast-enhanced 3D MRA using SENSE. J Magn Reson Imaging. 2000; 12:671–677. [PubMed: 11050636]
24. Golay X, Brown SJ, Itoh R, Melhem ER. Time-resolved contrast-enhanced carotid MR angiography using sensitivity encoding (SENSE). AJNR Am J Neuroradiol. 2001; 22:1615–1619. [PubMed: 11559518]
25. Wilson GJ, Hoogeveen RM, Willinek WA, Muthupillai R, Maki JH. Parallel imaging in MR angiography. Top Magn Reson Imaging. 2004; 15:169–185. [PubMed: 15479999]
26. Gauvrit JY, Leclerc X, Oppenheim C, Munier T, Trystram D, Rachdi H, Nataf F, Pruvo JP, Meder JF. Three-dimensional dynamic MR digital subtraction angiography using sensitivity encoding for the evaluation of intracranial arteriovenous malformations: a preliminary study. AJNR Am J Neuroradiol. 2005; 26:1525–1531. [PubMed: 15956525]
27. Frydrychowicz A, Bley TA, Winterer JT, Harloff A, Langer M, Hennig J, Markl M. Accelerated time-resolved 3D contrast-enhanced MR angiography at 3T: clinical experience in 31 patients. MAGMA. 2006; 19:187–195. [PubMed: 16937136]
28. Weiger M, Pruessmann KP, Boesiger P. 2D SENSE for faster 3D MRI. MAGMA. 2002; 14:10–19. [PubMed: 11796248]
29. Meckel S, Mekle R, Taschner C, Haller S, Scheffler K, Radue EW, Wetzel SG. Time-resolved 3D contrast-enhanced MRA with GRAPPA on a 1.5-T system for imaging of craniocervical vascular disease: initial experience. Neuroradiology. 2006; 48:291–299. [PubMed: 16532336]
30. Hadizadeh, DR.; Gieseke, J.; Hoogeveen, R.; von Falkenhausen, M.; Meyer, B.; Urbach, H.; Schild, H.; Willinek, WA. 4D Time-resolved angiography with CENTRA keyhole (4D-TRAK) and SENSE using a total acceleration factor of 60 as compared with catheter angiography in patients with cerebral arteriovenous malformations at 3.0T. Proceedings of the 14th Meeting of ISMRM; Seattle, WA. 2006. p. 807
31. Haider, CR.; Hu, HH.; Madhuranthakam, AJ.; Kruger, DG.; Campeau, NG.; Huston, J., 3rd; Riederer, SJ. Time-resolved 3D contrast-enhanced MRA with 2D homodyne and view sharing for contrast bolus dynamics of the brain. Proceedings of the 14th Meeting of ISMRM; Seattle, WA, USA. 2006. p. 812
32. Mende KA, Froehlich JM, von Weymarn C, Hoogeveen R, Kistler T, Zollikofer CL, Wentz KU. Time-resolved, high-resolution contrastenhanced MR angiography of dialysis shunts using the CENTRA key-hole technique with parallel imaging. J Magn Reson Imaging. 2007; 25:832–840. [PubMed: 17345633]
33. Hadizadeh DR, von Falkenhausen M, Gieseke J, Meyer B, Urbach H, Hoogeveen R, Schild HH, Willinek WA. Cerebral arteriovenous malformation: Spetzler-Martin classification at subsecond-

temporal-resolution four-dimensional MR angiography compared with that at DSA. Radiology. 2008; 246:205–213. [PubMed: 17951352]

34. Haider CR, Hu HH, Campeau NG, Huston J 3rd, Riederer SJ. 3D high temporal and spatial resolution contrast-enhanced MR angiography of the whole brain. Magn Reson Med. 2008; 60:749–760. [PubMed: 18727101]
35. Haider CR, Glockner JF, Stanson AW, Riederer SJ. Peripheral vasculature: high-temporal- and high-spatial-resolution three-dimensional contrast-enhanced MR angiography. Radiology. 2009; 253:831–843. [PubMed: 19789238]
36. Haider, CR.; Huston, J., 3rd; Campeau, NG.; Glockner, JF.; Stanson, AW.; Riederer, SJ. Max CAPR: high temporal and spatial resolution 3D CEMRA with scan times under five seconds. Proceedings of the 17th Annual Meeting of ISMRM; Honolulu, HI. 2009. p. 3786
37. Bernstein MA, Fain SB, Riederer SJ. Effect of windowing and zero-filled reconstruction of MRI data on spatial resolution and acquisition strategy. J Magn Reson Imaging. 2001; 14:270–280. [PubMed: 11536404]
38. Noll DC, Nishimura DG, Macovski A. Homodyne detection in magnetic resonance imaging. IEEE TMI. 1991; 10:154–163.
39. Hu HH, Madhuranthakam AJ, Kruger DG, Glockner JF, Riederer SJ. Combination of 2D sensitivity encoding and 2D partial Fourier techniques for improved acceleration in 3D contrast-enhanced MR angiography. Magn Reson Med. 2006; 55:16–22. [PubMed: 16342155]
40. Mostardi PM, Haider CR, Rossman PJ, Borisch EA, Riederer SJ. Controlled experimental study depicting moving objects in view-shared time-resolved 3D MRA. Magn Reson Med. 2009; 62:85–95. [PubMed: 19319897]
41. Borisch, EA.; Grimm, RC.; Rossman, PJ.; Haider, CR.; Riederer, SJ. Real-time high-throughput scalable MRI reconstruction via cluster computing. Proceedings of the 16th Annual Meeting of ISMRM; Toronto, Ontario, Canada. 2008. p. 1492
42. Rosner, B. Fundamentals of biostatistics. Belmont, CA: Duxbury Thomson Learning; 2005.
43. Du J, Carroll TJ, Wagner HJ, Vigen K, Fain SB, Block WF, Korosec FR, Grist TM, Mistretta CA. Time-resolved, undersampled projection reconstruction imaging for high-resolution CE-MRA of the distal runoff vessels. Magn Reson Med. 2002; 48:516–522. [PubMed: 12210917]
44. Wu Y, Korosec FR, Mistretta CA, Wieben O. CE-MRA of the lower extremities using HYPR stack-of-stars. J Magn Reson Imaging. 2009; 29:917–923. [PubMed: 19306427]
45. Brooks RA, Di Chiro G. Principles of computer assisted tomography (CAT) in radiographic and radioisotopic imaging. Phys Med Biol. 1976; 21:689–732. [PubMed: 788005]
46. O'Halloran RL, Wen Z, Holmes JH, Fain SB. Iterative projection reconstruction of time-resolved images using highly-constrained back-projection (HYPR). Magn Reson Med. 2008; 59:132–139. [PubMed: 18058939]
47. Meaney JF, Ridgway JP, Chakraverty S, Robertson I, Kessel D, Radjenovic A, Kouwenhoven M, Kassner A, Smith MA. Stepping-table gadolinium-enhanced digital subtraction MR angiography of the aorta and lower extremity arteries: preliminary experience. Radiology. 1999; 211:59–67. [PubMed: 10189454]
48. Vogt FM, Ajaj W, Hunold P, Herborn CU, Quick HH, Debatin JF, Ruehm SG. Venous compression at high-spatial-resolution three-dimensional MR angiography of peripheral arteries. Radiology. 2004; 233:913–920. [PubMed: 15486208]
49. Nael K, Fenchel M, Salamon N, Duckwiler GR, Laub G, Finn JP, Villablanca JP. Three-dimensional cerebral contrast-enhanced magnetic resonance venography at 3.0 tesla: initial results using highly accelerated parallel acquisition. Invest Radiol. 2006; 41:763–768. [PubMed: 16971800]
50. Cashen TA, Carr JC, Shin W, Walker MT, Futterer SF, Shaibani A, McCarthy RM, Carroll TJ. Intracranial time-resolved contrast-enhanced MR angiography at 3T. AJNR Am J Neuroradiol. 2006; 27:822–829. [PubMed: 16611772]
51. Griswold MA, Jakob PM, Chen Q, Goldfarb JW, Manning WJ, Edelman RR, Sodickson DK. Resolution enhancement in single-shot imaging using simultaneous acquisition of spatial harmonics (SMASH). Magn Reson Med. 1999; 41:1236–1245. [PubMed: 10371457]

52. Riederer SJ, Hu HH, Kruger DG, Haider CR, Campeau NG, Huston J 3rd. Intrinsic signal amplification in the application of 2D SENSE parallel imaging to 3D contrast-enhanced elliptical centric MRA and MRV. Magn Reson Med. 2007; 58:855–864. [PubMed: 17969124]

53. Hu HH, Campeau NG, Huston J 3rd, Kruger DG, Haider CR, Riederer SJ. High-spatial-resolution contrast-enhanced MR angiography of the intracranial venous system with fourfold accelerated two-dimensional sensitivity encoding. Radiology. 2007; 243:853–861. [PubMed: 17446523]

54. Tsao J, Boesiger P, Pruessmann KP. k-t BLAST and k-t SENSE: dynamic MRI with high frame rate exploiting spatiotemporal correlations. Magn Reson Med. 2003; 50:1031–1042. [PubMed: 14587014]

55. Johnson KM, Velikina J, Wu Y, Kecskemeti S, Wieben O, Mistretta CA. Improved waveform fidelity using local HYPR reconstruction (HYPR LR). Magn Reson Med. 2008; 59:456–462. [PubMed: 18306397]

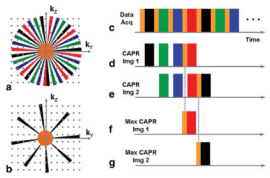

FIG. 1.

Comparison of the sampling patterns of the k_Y-k_Z phase encoding plane for the Cartesian CAPR technique **(a)** and the non-view-shared Max CAPR technique **(b). c:** Temporal play-out of phase-encoding measurements used for both CAPR and Max CAPR. **d,e:** Selection of the data from **(c)** for formation of images 1 and 2 for the CAPR sequence. **f,g:** Selection of data for formation of images 1 and 2 for the Max CAPR sequence. The same sampling of the central orange region is used for corresponding CAPR and Max CAPR images.

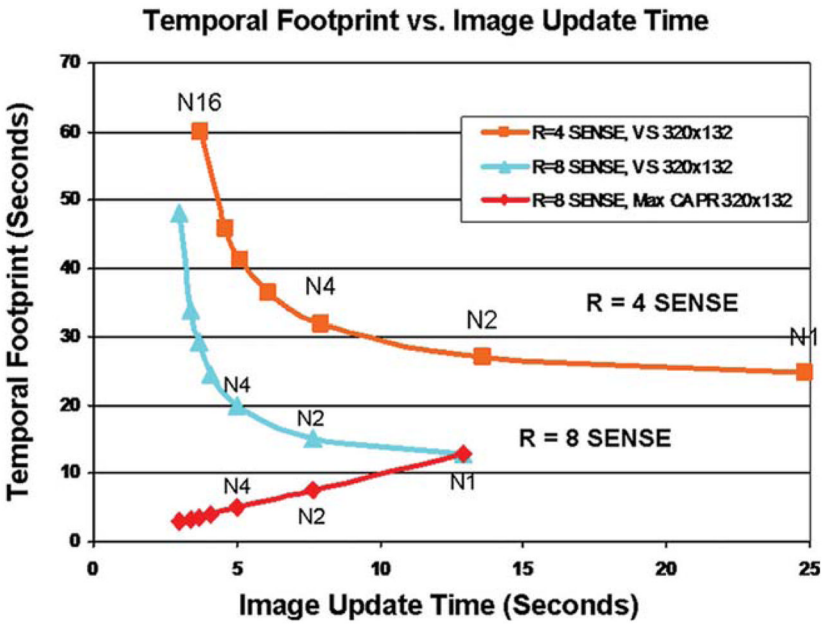

FIG. 2.

Plot of temporal footprint versus image update time for fixed Y × Z sampling of 320 × 132. Curves are shown for SENSE accelerations *R* = 4 and 8. The parameter N1, N2, etc. corresponds to increased degrees of view sharing, providing a reduced update time but increased temporal footprint. For Max CAPR (red line) no view sharing is performed, and so the update time matches the temporal footprint. For much of this work, N4 Max CAPR was studied.

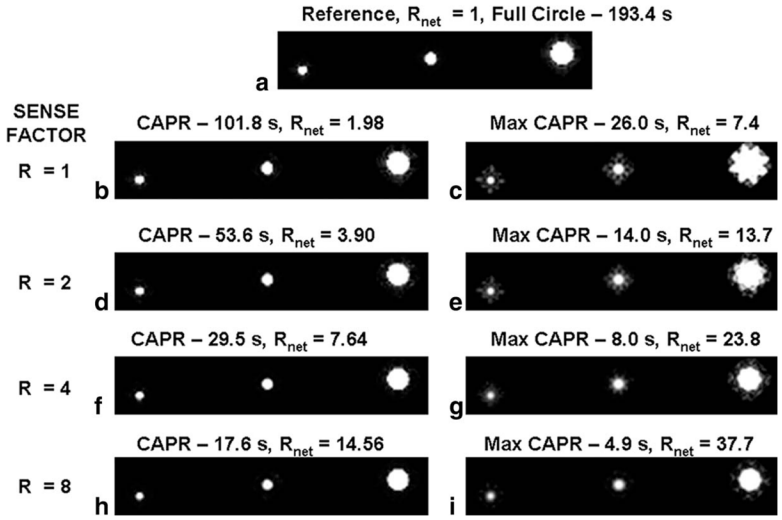

FIG. 3.

Axial slices of three tubes of diameter 3, 5, and 7mm acquired with increasing acceleration. **a:** Image from fully sampled k_Y-k_Z-space. Acquisition time was 193.3 sec. **b,d,f,h:** Reference CAPR reconstructions formed using 2D HD and the SENSE accelerations (R) shown. For each case, the acquisition time and the net acceleration R_{net} versus **(a)** are indicated. **c,e,g,i:** Max CAPR images reconstructed from the same respective data sets as for CAPR but using only one of the four vane sets. For each, the acquisition time and R_{net} are given.

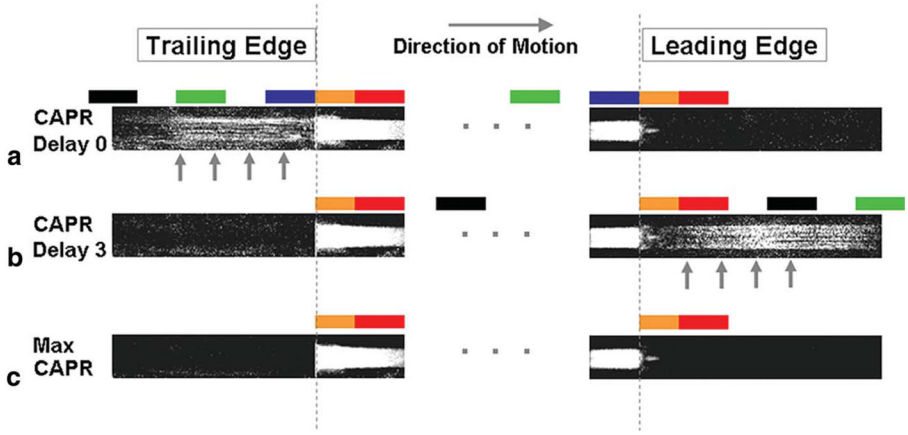

FIG. 4.

Enlargements of the leading and trailing edges of the moving phantom, each from distinct timeframes, for **(a)** CAPR Delay 0, **(b)** CAPR Delay 3, and **(c)** Max CAPR reconstructions. For each case, the colored blocks indicate which region of *k*-space is being sampled at the instant the bolus edge is at the position within the block. Note that CAPR Delay 0 has substantial persistence artifact (**(a)**, arrow), CAPR Delay 3 has substantial anticipation artifact (**(b)**, arrow), but Max CAPR **(c)** has negligible artifact in advance of and trailing the bolus edges.

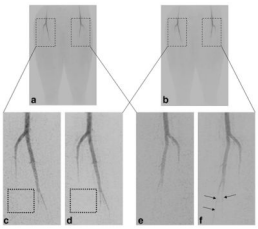

FIG. 5.

Comparison of CAPR (17.6-sec acquisition time) and Max CAPR (4.9-sec acquisition time). Full coronal MIP images of **(a)** CAPR and **(b)** Max CAPR results showing the leading edge of contrast material as it enters the proximal portion of the lower legs over the full FOV. Enlargements of the right leg of CAPR **(c)** and Max CAPR **(d)** portray the bifurcation of the popliteal artery. Note the increased noise level within the dashed box for CAPR **(c)** versus Max CAPR **(d)**. Enlargements of the left leg from CAPR **(e)** and Max CAPR **(f)** illustrate improved sharpness in portraying the leading edge of the contrast bolus for Max CAPR (**(f)**, arrows).

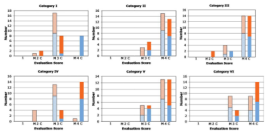

FIG. 6.

Plots of the evaluation scores of the nine patient studies for each of the six categories defined in Table 2. For each category, results are shown for the two reviewers, a total of 18 scores for Max CAPR and 18 scores for CAPR.

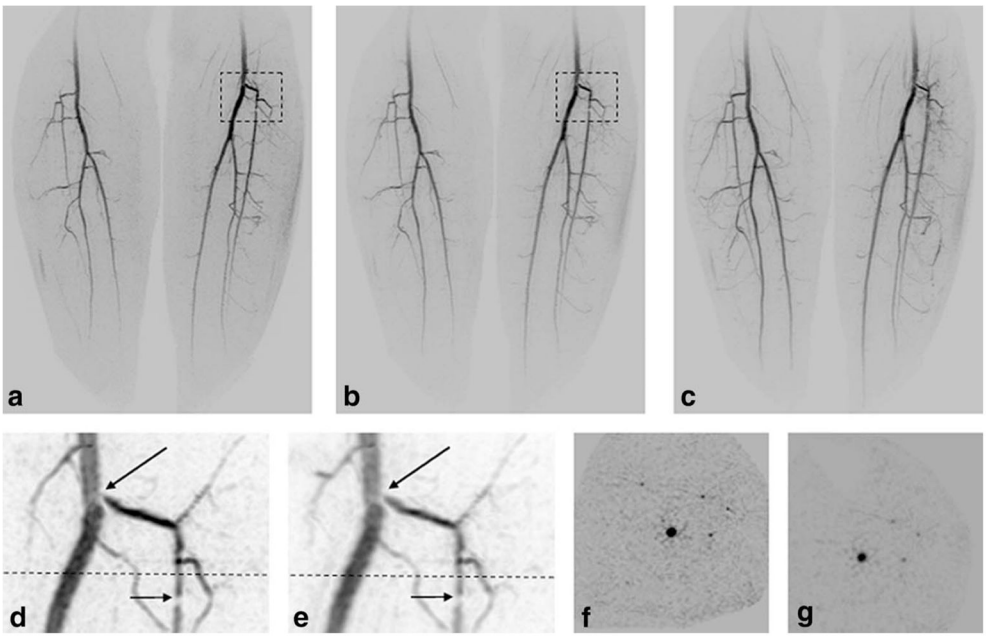

FIG. 7.

Comparison of CAPR (17.6-sec acquisition time) versus Max CAPR (4.9-sec acquisition time) from a patient study. Coronal MIP of full FOV of CAPR **(a)** and Max CAPR **(b)** for the frame when contrast material nominally fills the arteries within the calves. **c:** Max CAPR result one timeframe (4.9 sec) later than **(b)**. Comparison of **(d)** CAPR and **(e)** Max CAPR subvolumes of the left popliteal bifurcation (dashed boxes in **(a)** and **(b)**) shown at an oblique angle to better portray the two stenotic areas, one at the origin of the anterior popliteal artery (long arrow, **(d)** and **(e)**), the second several centimeters distal (short arrow, **(d)** and **(e)**). Although the Max CAPR result is slightly blurred versus CAPR, it still portrays the pathology well. Axial images of CAPR **(f)** and Max CAPR **(g)** taken from the level of the dashed lines from the respective subvolumes of **(d)** and **(e)** show the dark vessel lumens. Note the increased noise level in the background of CAPR. See also Supplementary Videos V1 and V2.

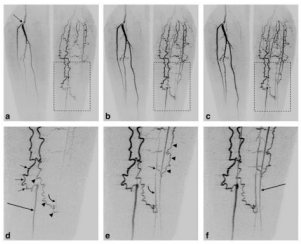

FIG. 8.

Illustration from a patient study of the spatial and temporal resolution of Max CAPR (4.9-sec acquisition time). **a–c:** Coronal MIPs of consecutive 4.9-sec timeframes in a patient having a lesion at the origin of the right popliteal bifurcation (arrow, **(a)**) and filling via collateral vessels of the vasculature of the left leg. **d–f:** Enlargements from the region of the left leg (dashed boxes, **(a–c)**), allowing delineation of the filling patterns. **d:** Filling of the native distal left posterior tibial artery (long arrow, **(d)**) is done via a medial collateral vessel (short arrows, **(d)**). Second collateral vessel (arrowheads, **(d)**) spontaneously anastomoses to a distal native peroneal artery, with an early hint of retrograde flow (curved arrow, **(d)**). **e:** Subsequent frame shows further retrograde flow along peroneal artery (curved arrow, **(e)**), as well as a more proximal anastomosis in the peroneal artery (short arrow, **(e)**) from a third collateral vessel (arrowheads, **(e)**). **f:** Next frame shows further enhancement, including filling of native left anterior tibial artery (long arrow, **(f)**). See also Supplementary Videos V3 and V4.

Table 1

Imaging Parameters for Experimental Studies*

Imaging parameters	Phantom experiments parameters						In vivo parameters, 8 × calves
	Full ref.	Circular ref.	CAPR ref.				
TR/TE (msec)	5.9/2.7	5.9/2.7	5.9/2.7				5.9/2.7
Flip angle (degrees)	30	30	30				30
Bandwidth (± kHz)	62.5	62.5	62.5				62.5
Sampling matrix (Nx × Ny × Nz)	400 × 320 × 132	400 × 320 × 132	400 × 320 × 132				400 × 320 × 132
FOV (X × Y × Z cm^3)	40 × 32 × 13.2	40 × 32 × 13.2	40 × 32 × 13.2				40 × 32 × 13.2
Spatial resolution (X × Y × Z cm^3)	1 × 1 × 1	1 × 1 × 1	1 × 1 × 1				1 × 1 × 1
CAPR specific parameters							
Center size	42,240	32,788	400				400
View sharing	N1	N1	N4				N4
CAPR HD undersampling factor (R_{HD})	0.78	1	1.98	1.95	1.91	1.82	1.82
2D SENSE acceleration (R)			1	2	4	8	8
R_{net} CAPR = R_{HD} × R	0.78	1	1.98	3.9	7.64	14.56	14.56
Max CAPR undersampling (R_{US})			3.73	3.5	3.12	2.59	2.59
R_{net} Max CAPR = R_{HD} × R × R_{US}			7.39	13.65	23.84	37.7	37.7
Temporal footprint (sec)							
CAPR	249.2	193.4	101.8	53.6	29.5	17.6	17.6
Max CAPR			26	14	8	4.9	4.9
Frame time (sec)							
CAPR	249.2	193.4	26	14	8	4.9	4.9
Max CAPR			26	14	8	4.9	4.9
Associated figure		3	3				4, 5, 7, 8

*The Full ref. column is for the case in which a full rectangular region in k_Y-k_Z space of Ny × Nz points is sampled. For the Circular ref. case, the corners of k_Y-k_Z space are not sampled, as discussed in the text. The parameter "Nm" for view-sharing indicates that "m" vane sets are used. The set of four values listed in the CAPR ref. column for each of R_{HD}, R, R_{US}, R_{net} CAPR, R_{net} Max CAPR, temporal footprint, and frame time is for respective SENSE accelerations of *R* = 1, 2, 4, 8.

Table 2

Review Criteria and Definition of Scores for Radiological Evaluation of Patient Studies

Review categories	
I. Image artifacts as a result of noise, motion, undersampling, or aliasing	
1	Severe. Nondiagnostic.
2	Moderate. May interfere with diagnosis.
3	Minor. Will not interfere with diagnosis.
4	None
II. Arterial-to-venous separation	
1	Severe. Extensive mixing of venous with arterial signal or vice versa.
2	Moderate. Probably will interfere with diagnosis.
3	Mild. Venous contamination will not confound diagnosis.
4	Excellent. Multiple clear arterial frames prior to venous filling, with crisp, clear progression from arterial to venous phase.
III. Continuity of arterial signal of major vessels	
1	Poor. Lack of uniform signal.
2	Mild. Variation in signal intensity.
3	Good. Minor variations that will not interfere with diagnosis.
4	Excellent. Vessels have uniform signal along the vessel.
IV. Vessel sharpness	
1	Poor. Vessels have poor spatial resolution with little or no structure.
2	Mild. Slight blurring of vessels that probably will not affect diagnosis.
3	Good. Any blur will not interfere with diagnosis.
4	Excellent. Crisp detail with adequate spatial resolution to visualize vessels of interest.
V. Leading edge of arterial signal of major vessels	
1	Poor. Leading edge is poorly seen because of poor signal or spatial resolution.
2	Mild. Variation in signal intensity or spatial resolution that can potentially confound diagnosis.
3	Good. Minor variations that will not interfere with diagnosis.
4	Excellent. Leading edge is well seen.
VI. Overall image quality	
1	Nondiagnostic
2	Marginal
3	Good
4	Excellent

Table 3

Results of Radiological Evaluation, Aggregate for the Two Reviewers

Category	I	II	III	IV	V	VI
Max CAPR						
Mean ± standard deviation	2.94 ± 0.24	3.83 ± 0.38	3.78 ± 0.43	2.83 ± 0.51	3.72 ± 0.46	3.50 ± 0.51
Significance vs. marginal examination	P < 0.0001	P < 0.0001	P < 0.0001	P < 0.0001	P < 0.0001	P < 0.0001
CAPR						
Mean ± standard deviation	3.33 ± 0.69	3.72 ± 0.46	3.67 ± 0.69	3.78 ± 0.43	3.72 ± 0.46	3.78 ± 0.43
Significance vs. marginal examination	P < 0.0001	P < 0.0001	P < 0.0001	P < 0.0001	P < 0.0001	P < 0.0001
Max CAPR vs. CAPR	CAPR superior	n.s.	n.s.	CAPR superior.	n.s.	n.s.
Significance	P < 0.05			P < 0.05		